A Unified Circuit View of Multiphysics Finite Element Analysis via Discrete Exterior Calculus Part II: 2D Dynamic Fields

Mehran Keivanimehr
University of Florida
Gainesville, FL, USA
m.keivanimehr@ufl.edu

Baoyun Ge, *Member, IEEE*
Georgia Institute of Technology
Atlanta, GA, USA
baoyun.ge@ece.gatech.edu

***Abstract*—Engineering challenges often necesssitate multiphysics integration. However, different physical processes in engineering systems are described with languages often only comprehensible by engineers in respective disciplines. This paper is bridging the gaps between multiphysics in finite element analysis (FEA) formulations through a unified circuit view. This unification is systematically done via a mathematical tool called discrete exterior calculus (DEC). It will not help with the FEA computationally, rather it will give the designers an intuitive and unified perspective about the multiphysics in engineering systems and potentially lead to novel multiphysics design approaches. This paper is a multi-part effort. Here we present Part II focusing on 2D dynamic fields.**

***Keywords*—circuit, discrete exterior calculus, multiphysics**

I. Introduction

Engineering challenges often necessitate multiphysics integration, which refers to the simultaneous consideration of multiple physical processes interacting with each other within a system. For example, multiphysics integration is frequently sought when designing electric motors and generators, or collectively electric machines (EMs). For example, in electric machines, heat pipes are integrated with hollow conductors to promptly reject heat [1], [2], the axial flow compression is integrated with the rotor of an electric machine to achieve higher density [3], structural mechanics are co-designed with the electromagnetics to maximize power density for rare-earth free electric machines [4], [5], radial forces in electric machines are leveraged to get rid of bearings for high efficiency and reliability [6]–[8], etc. More examples can be found in other engineering objects, such as wireless power transfer devices [9]–[11], magnetohydrodynamic pumps [12], [13], power modules [14]–[16], etc.

These processes governing the physical world include acoustics, heat transfer, fluid dynamics, solid deformation, electromagnetics, etc. They are described by partial differential equations (PDEs). However, these processes and PDEs are often taught separately in various departments and multiple courses of engineering, making them difficult for students outside of the specific discipline to comprehend. This curriculum setting forms language barriers among engineers of different backgrounds and does not help with multiphysics integration.

This paper is a multi-part effort and tries to break these language barriers by unifying the view of multiphysics finite element analysis. The intuition comes from the fact that engineers often use analogy to understand different disciplines. For example, concepts like magnetic reluctance, spring stiffness, thermal resistance, and pipe bore constriction can be related to the resistance concept in circuit theory. Part I presented in [17] was focused on 2D static fields and the derivation of the circuit formulation of multiphysics was supported by discrete exterior calculus (DEC) [18]–[22] and finite element analysis (FEA) [23], [24].

Part II of this effort is focused on 2D dynamic (i.e., dependent on time and independent of the third dimension) fields. Our work in Part II is built upon Part I and adds time-varying components to the PDEs, DEC formulations, and eventually circuit models. In static fields, materials exhibit static stiffness to loads and the stiffness is captured by resistors (resistance or conductance) in the circuit view. While in dynamic fields, materials exhibit dynamic stiffness to changing loads and energy may be temporarily stored and released locally. Hence, circuit devices like inductors and capacitors show up in equivalent circuit models.

Interested readers may refer to Part I for our motivation and intuition coming from topology optimization. Furthermore, the topological structure established by DEC and circuit theory to hint on the possibility of viewing FEA as solving a circuit network was presented in Part I and will be omitted. The rest of the paper is organized as follows: Section II presents a case study using electric machines as an example and two physical processes (eddy current field and dynamic thermal conduction) are used to illustrate the unified circuit view; Section III documents benchmark results of the DEC formulation against a commercial software package (COMSOL Multiphysics). Moreover, we constructed and validated circuit models in NgSpice, which is a variant of the well known circuit simulator SPICE. Sections IV and V outlines plans for follow-up work and concludes the findings of the this research.

This work was partially supported by the U.S. National Science Foundation Award #2338541.

II. A Case Study of Dynamic Physical Processes in Electric Machines

In this section, we will use two 2D dynamic physical processes involved in EMs to illustrate the unified circuit view. Particularly, we present circuits depicting eddy current (Figure 2) and thermal conduction (Figure 4). The study on elastic fields will be included in the expanded version of this work. It is worth mentioning that the eddy current in the frequency domain has been studied in Part I. Herein, we focus on time-domain eddy current fields.

A. Eddy Current

We will show the DEC formulation for eddy current fields. It is governed by a variant of the Ampère's Law:

$$\nabla \cdot \left(\nabla \frac{1}{\mu} A_z \right) = -J_z \tag{1}$$

and a combination of the Faraday's Law and Ohm's Law:

$$J_z = \sigma E_{\text{ext}} - \sigma \frac{\partial A_z}{\partial t} \tag{2}$$

where A_z is the z-component of the vector potential, J_z is the z-component of the current density, μ is material permeability, σ is electrical conductivity, and E_{ext} is the externally applied electric field.

The DEC formulation of eq. (1), which has been presented in Part I, is copied below for convenience.

$$\sum_j \left(\frac{2}{\mu_l} \frac{\left|e_{ij}^\star\right|_l}{|e_{ij}|} + \frac{2}{\mu_r} \frac{\left|e_{ij}^\star\right|_r}{|e_{ij}|} \right) \left(\widetilde{A}_{z,j} - \widetilde{A}_{z,i} \right) = -2 \left|C_i\right| \widetilde{J}_{z,i} \tag{3}$$

The tildes indicate that the variables underneath are discrete differential forms instead of scalars/vectors normally understood in vector calculus. The symbol e_{ij} means the edge connecting vertices i and j, $e_{ij}^\star$ is the dual space of e_{ij}, and C_i represents the dual space of vertex i. The vertical bars around these symbols designates their corresponding sizes (length, area, *etc.*). The subscripts l and r denote the two simplicial meshes (*i.e.* triangles) adjacent to the edge connected by vertices i and j.

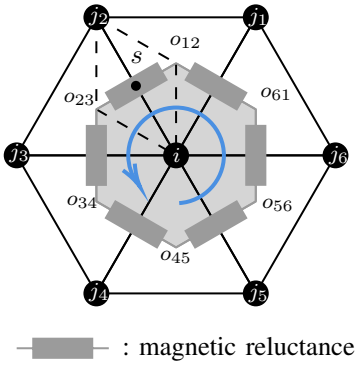

Fig. 1: Magnetostatic circuit network centered around the vertex i. A regular hexagon is used for drawing convenience.

The corresponding circuit model is duplicated as well in Figure 1. It can be seen that magnetic reluctance, which corresponds to the terms in the parenthesis of eq. (2) and is a concept used in macroscopic modeling of inductors, transformers, and EMs, shows up at the mesh level (microscopic view). Furthermore, the total MMF drop around a closed loop equals the total current enclosed by the same loop, resembling the behavior of magnetic circuit known to power engineers. This connection between macroscopic and microscopic views of physical processes is particularly interesting and worth exploring in order to help engineers quickly develop intuitions into multiphysics.

For the time-domain eddy current we are considering here, eq. (2) has to be incorporated into the circuit. For one thing, in magnetostatic fields current distribution is usually given, while in eddy current problems it is usually the externally applied voltage that is forced. To achieve the incorporation, we discretize eq. (2) and substitute it into the right-hand-side (RHS) of eq. (3):

$$\sum_j \left(\frac{2}{\mu_l} \frac{\left|e_{ij}^\star\right|_l}{|e_{ij}|} + \frac{2}{\mu_r} \frac{\left|e_{ij}^\star\right|_r}{|e_{ij}|} \right) \left(\widetilde{A}_{z,j} - \widetilde{A}_{z,i} \right) = -2 \left|C_i\right| \sigma \widetilde{E}_{\text{ext},i} + 2 \left|C_i\right| \sigma \frac{\partial \widetilde{A}_{z,i}}{\partial t} \tag{4}$$

To convert eq. (4) into an equivalent circuit, we may view the first term of the RHS as a voltage source and the second term as the voltage across an inductor (instead of capacitor, since A_z is modeled as current rather than voltage in the circuit). Similar to μ_l and μ_r accounting for different materials, these terms may be further partitioned to capture discontinuities in electrical conductivity. Since series connected inductors can be lumped together, these partitioned terms may be represented by one inductor.

Figure 2 depicts such an equivalent circuit. In this circuit, each impedance (represented in rectangular gray objects) is more than just the magnetic reluctance in Figure 1. It contains two voltage sources as well as an inductor. One of the voltage

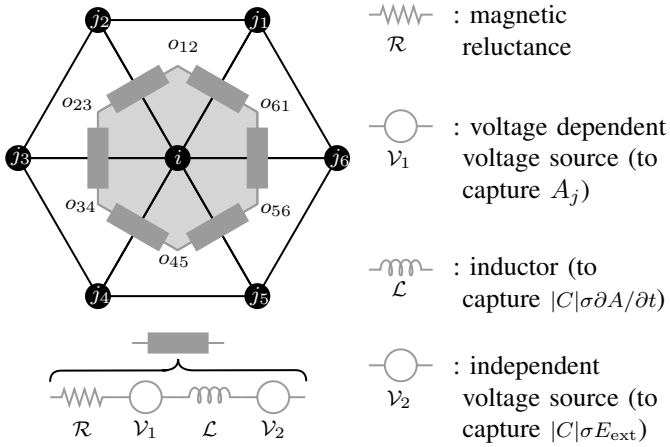

Fig. 2: Eddy current circuit network centered around the vertex i.

source is for modeling MMF contribution from adjacent vertices. This voltage source and the reluctance together models the MMF drop due to flux passing through the edge e_{ij}. As has been mentioned in Part I, it is the line integration of vector potential that has the meaning of flux per axial length. Another voltage source captures the externally enforced current. If it was not for the Faraday's Law or the source is purely DC, this voltage source would be equivalent to the blue arrow in Figure 1. Lastly, the inductor models the essence of the Faraday's Law, i.e. a changing magnetic vector potential (*i.e.* current in the equivalent circuit) will induce a current density (*i.e.* induced voltage across the inductor in the equivalent circuit) opposing such a change. Notice that the inductor $\mathcal{L}$ is not the typical inductor we use in modeling parasitics of electrical wires and it has a unit of $\mathrm{S}\cdot\mathrm{m}$. Unlike the first two circuit elements relating to both vertices i and j, the inductor and the independent voltage source are tied with vertex i only.

Interestingly, recently several researchers worked on a macroscopic equivalent circuit that captures the dynamic behavior of eddy currents and it adds a circuit element called magductance (or magnetic inductance) to conventional magnetic circuits [25]. Although the inductor $\mathcal{L}$ in Figure 2 has a unit different from magductance, it can be shown that they are capturing the same physical phenomenon. This again confirms that physical processes under lens of different magnification have similar structures in equivalent circuit models.

B. Dynamic Thermal Conduction

Next, we will show the DEC formulation for dynamic thermal conduction field. It is governed by

$$\nabla\cdot(\nabla kT) = -q_h + \rho c_p \frac{\partial T}{\partial t} \tag{5}$$

where k is thermal conductivity, T is temperature, q_h is injected heat flux, ρ is material density, and c_p is specific heat capacity. Compared with the steady-state version, eq. (5) contains a dynamic term that captures how thermal energy stored and released from the material. This energy is proportional to ρc_p with a unit of $\mathrm{J}/\mathrm{m}^3\cdot\mathrm{K}$.

The DEC formulation of the steady-state thermal conduction fields, which has been presented in Part I, is copied below for convenience.

$$\sum_j \left(k_l \frac{\left|e^\star_{ij}\right|_l}{2\left|e_{ij}\right|} + k_r \frac{\left|e^\star_{ij}\right|_r}{2\left|e_{ij}\right|} \right) \left(\widetilde{T}_j - \widetilde{T}_i\right) = -\frac{1}{2}\left|C_i\right| \widetilde{q}_{h,i} \tag{6}$$

The corresponding circuit model is duplicated as well in Figure 3. As in magnetostatic fields, the macroscopic concept, i.e. thermal resistance or conductance, known to engineers shows up in the microscopic view. Comparing Figure 3 to Figure 1, there is an obvious difference between them. Figure 1 shows that magnetostatic field naturally forms a mesh-type network, while Figure 3 shows that the thermal conduction naturally forms a nodal-type network. This is expected as magnetic flux is perpendicular to the vector potential field $\mathbf{A}$, while heat flux is in line with the temperature gradient ∇T.

Incorporating the dynamic term in eq. (5) into the DEC formulation, one would obtain

$$\sum_j \left(k_l \frac{\left|e^\star_{ij}\right|_l}{2\left|e_{ij}\right|} + k_r \frac{\left|e^\star_{ij}\right|_r}{2\left|e_{ij}\right|} \right) \left(\widetilde{T}_j - \widetilde{T}_i\right) = -\frac{1}{2}\left|C_i\right| \widetilde{q}_{h,i} + \frac{1}{2}\left|C_i\right| \rho c_p \frac{\partial \widetilde{T}_i}{\partial t} \tag{7}$$

To convert eq. (7) into an equivalent circuit, we may view the first term of the RHS as a current source and the second term as the current through a capacitor (instead of inductor, since T is modeled as voltage rather than current in the circuit). Similar to k_l and k_r accounting for different materials, the second term may be further partitioned to capture discontinuities in ρ and c_p. Since parallel capacitors can be grouped together, these partitioned terms may be represented by one capacitor.

The resultant equivalent circuit is presented in Figure 4. It is perhaps not as surprising as that in Figure 2. Compared with Figure 3, it only adds the capacitive branch to each vertex. In existing practices, engineers have applied the concept of thermal capacitance to model the dynamic behavior. Notice that unlike the eddy current fields, we introduced ground node to the circuit. This is due to the fact that the temperature T is modeled as voltage in the circuit and voltage usually

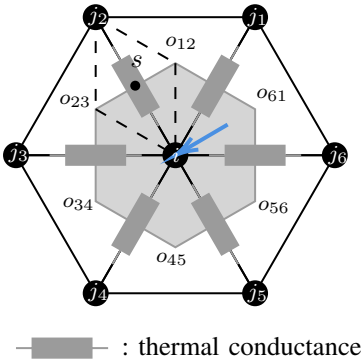

Fig. 3: Steady-state thermal circuit network centered around the vertex i.

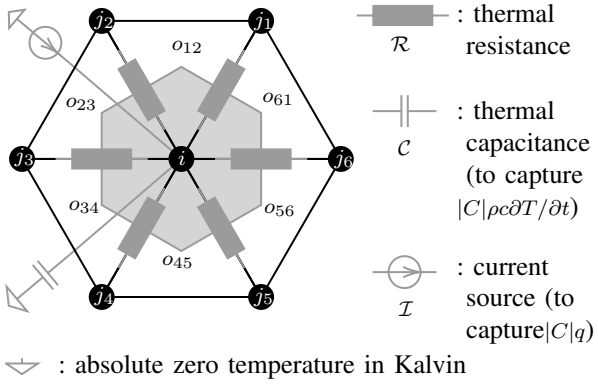

Fig. 4: Dynamic thermal circuit network centered around the vertex i.

has a reference. On the other hand, the ground node in the current source branch is immaterial and it is there merely for completing the circuit.

III. Experimental Results

To validate these equivalent circuit models, we designed two experiments. First, the DEC formulations presented in eqs. (4) and (7) were programmed and solved in Matlab. The results were benchmarked against that obtained using COMSOL Multiphysics. Second, the circuits in Figures 2 and 4 were constructed and solved in NgSpice. The results were compared with COMSOL. In this step, A_z and T were tracked while material properties were tweaked. Electrical engineers often enjoy using RC and RL time constants to quickly analyze circuit behaviors. Such a practice may be transferred to the equivalent circuits proposed herein.

A. Eddy Current

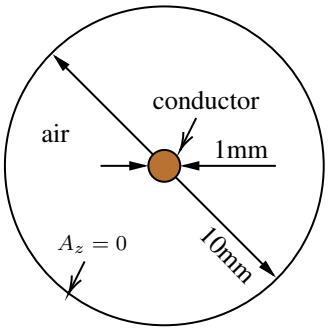

Fig. 5: Geometry of the simulated eddy current problem.

The geometry of the simulated eddy current problem is depicted in Figure 5. It includes a piece of conductor surrounded by air. The setup has an axial length of one meter. The conductor is made of copper ($\sigma = 59.6\,\mathrm{MS/m}$) and excited with an external AC voltage at a frequency of $50\,\mathrm{kHz}$ and an amplitude of $1\,\mathrm{V}$. The setup was simulated in COMSOL first and the resultant distribution of vector potential A_z when $t = 5\,\mu\mathrm{s}$ is given in Figure 6. Next, we feed the COMSOL solution to eq. (4) and compared the left-hand-side (LHS) with RHS. Since time was involved, the relative error between them are presented in two ways. The first one, plotted in Figure 7, shows the mean (over time) relative error over the

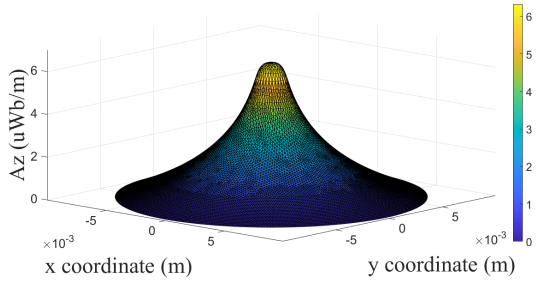

Fig. 6: Distribution of vector potential (from COMSOL) when $t = 5\,\mu\mathrm{s}$.

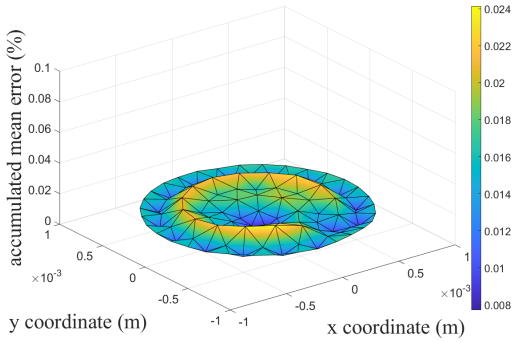

Fig. 7: Distribution of mean (over time) relative error of the LHS to RHS of eq. (4) by substituting COMSOL results.

spatial domain. The second one, plotted in Figure 8, exhibits the total (aggregated over copper region) relative error in the time domain. It can be seen that the relative error is high when the applied voltage is close to zero (i.e. when the rate of change is maximum). This may be related to how time derivative is approximated in COMSOL. Nevertheless, both plots demonstrate that the DEC formulation can accurately model eddy current fields. Notice that the relative error is only computed for the copper region. For the air region, since the conductivity is set to zero, RHS of eq. (4) is essentially zero, making relative error an ineffective metric.

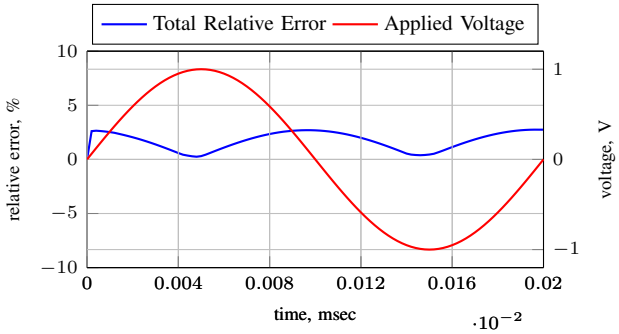

Fig. 8: Total (aggregated over copper region) relative error as a function of time.

Next, the circuit in Figure 2 was constructed and solved in NgSpice. A Python script that converts mesh and material information into a netlist that could be processed by NgSpice was created. The vector potential data (i.e. current in each loop) was extracted after the circuit was resolved by NgSpice and the data is compared with that obtained via COMSOL. Figure 9 presents such a comparison at three different radii (since the setup is axisymmetric, their angular positions are irrelevant). It can be seen that the data through NgSpice is in well agreement with that produced by COMSOL, indicating the correctness and high fidelity of the proposed circuit model.

Perhaps the most interesting experiment is the following. We changed the conductor material to titanium ($\sigma = 2.38\,\mathrm{MS/m}$) and carbon ($\sigma = 0.2\,\mathrm{MS/m}$) and extracted data from both COMSOL and NgSpice simulations at the same vertex. The

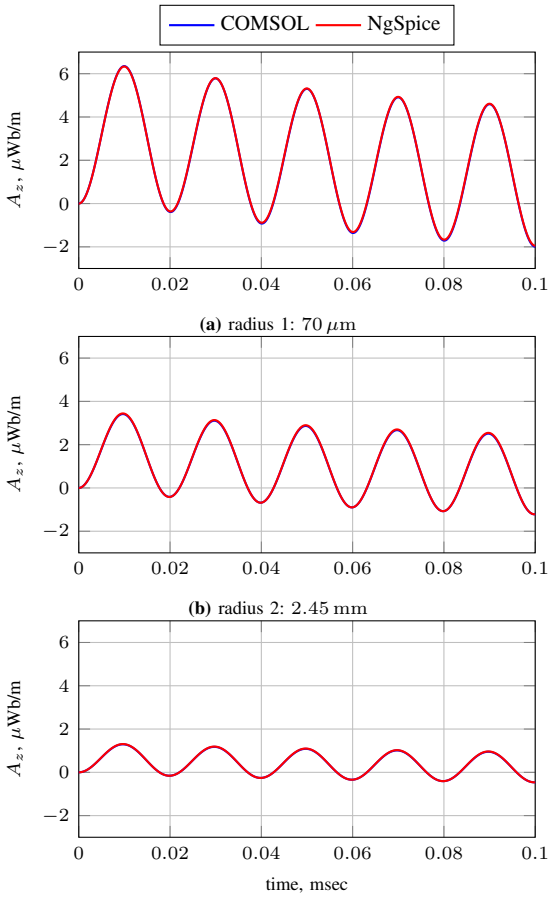

(a) radius 1: 70 μm

(b) radius 2: 2.45 mm

(c) radius 3: 5.88 mm

Fig. 9: Vector potential as a function of time at three different radii.

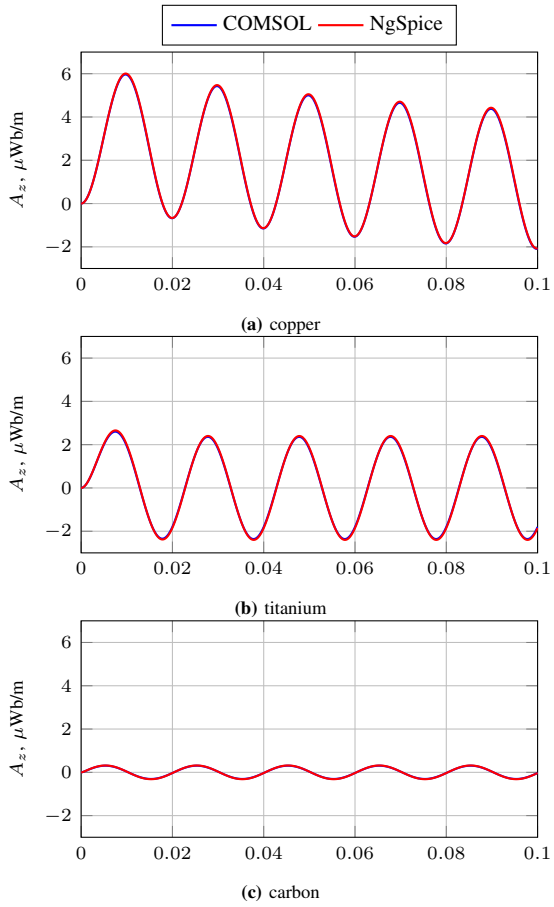

(a) copper

(b) titanium

(c) carbon

Fig. 10: Vector potential as a function of time with three different materials.

results are shown in Figure 10. It can be seen that as the conductivity decreased, the settling time of the exponentially decaying transients decreased as well. This can be quickly verified through the circuit model in Figure 2. The time constant of the circuit ($\mathcal{L}/\mathcal{R}$) is proportional to $\sigma\mu$. As the conductivity decreased, the time constant decreased as well, suggesting that it would take less time to settle down. Such an insight provided by the circuit view, however, is not easily attainable through directly reading PDEs (in this case Maxwell's equations). Notice that even though the amplitudes share similar trends among the waveforms in Figures 9 and 10, the settling time in Figure 9 are similar because the same material (copper) was used.

B. Dynamic Thermal Conduction

The geometry of the simulated thermal conduction problem is depicted in Figure 11. It is filled with one material. The setup has a length of one meter in the z direction. Both left and right sides of the block have unlimited thermal capability such that the left side has a fixed time-varying temperature $T(t) = 10\sin(100\pi t)+293.15\,\mathrm{K}$ and the right side has a fixed time-invariant temperature 273.15 K. The setup was simulated in COMSOL first and the resultant distribution of temperature T when $t = 0.5\,\mathrm{s}$ is given in Figure 12. Next, we feed the COMSOL solution to eq. (7) and compared the LHS with RHS. Like in Section III-A, the relative error between them are presented in two ways. The first one, plotted in Figure 13, shows the mean (over time) relative error over the spatial domain. The second one, plotted in Figure 14, exhibits the total (aggregated over copper region) relative error in the time domain. Nevertheless, both plots demonstrate that the DEC formulation can accurately model dynamic thermal conduction fields.

Next, the circuit in Figure 4 was constructed and solved in NgSpice. A Python script that converts mesh and material information into a netlist that could be processed by NgSpice was created. The temperature data (i.e. voltage at each vertex) was extracted after the circuit was resolved by NgSpice and the data is compared with that obtained via COMSOL. Fig-

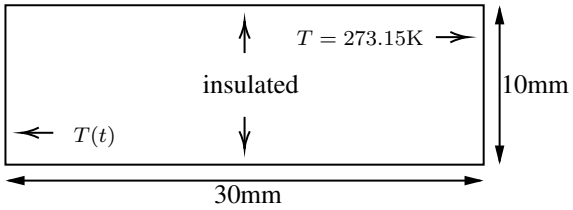

Fig. 11: Geometry of the simulated thermal conduction problem.

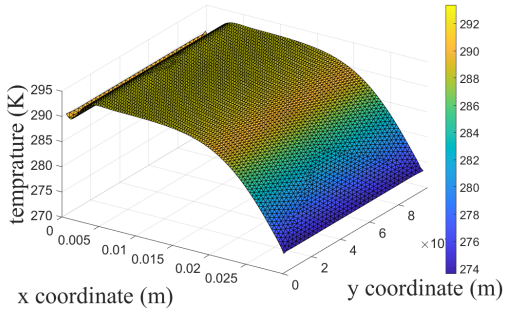

Fig. 12: Distribution of temperature (from COMSOL) when $t = 0.5\,\mathrm{s}$.

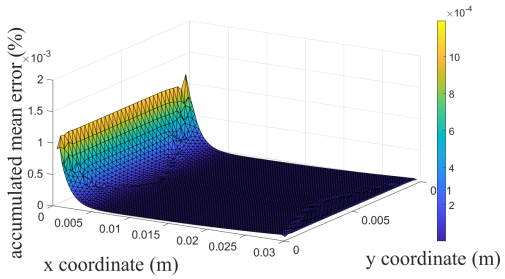

Fig. 13: Distribution of mean (over time) relative error of the LHS to RHS of eq. (7) by substituting COMSOL results.

ure 15 presents such a comparison at three different horizontal locations (since the top and bottom boundaries are thermally insulated, their y-coordinates are irrelevant). It can be seen that the data through NgSpice is in well agreement with that produced by COMSOL, indicating the correctness and high fidelity of the proposed circuit model.

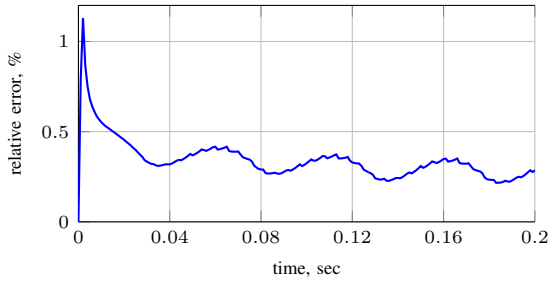

Fig. 14: Total (aggregated over the whole region) relative error as a function of time.

Like in Section III-A, the most interesting experiment is perhaps the following. We changed the material from copper ($k = 400\,\mathrm{W/(m \cdot K)}$, $\rho = 8960\,\mathrm{kg/m^3}$, $c_p = 385\,\mathrm{J/(kg \cdot K)}$) to diamond ($k = 2000\,\mathrm{W/(m \cdot K)}$, $\rho = 3510\,\mathrm{kg/m^3}$, $c_p = 502\,\mathrm{J/(kg \cdot K)}$) and lead ($k = 35\,\mathrm{W/(m \cdot K)}$, $\rho = 11340\,\mathrm{kg/m^3}$, $c_p = 128\,\mathrm{J/(kg \cdot K)}$) and extracted data from both COMSOL and NgSpice simulations at the same vertex. The results are shown in Figure 16. It can be seen that it took diamond less time and lead longer time to settle down. This can be quickly verified through the circuit model in Figure 4. The time constant of the circuit ($\mathcal{RC}$) is proportional to $\rho c_p/k$. The time constants of diamond and lead are respectively about

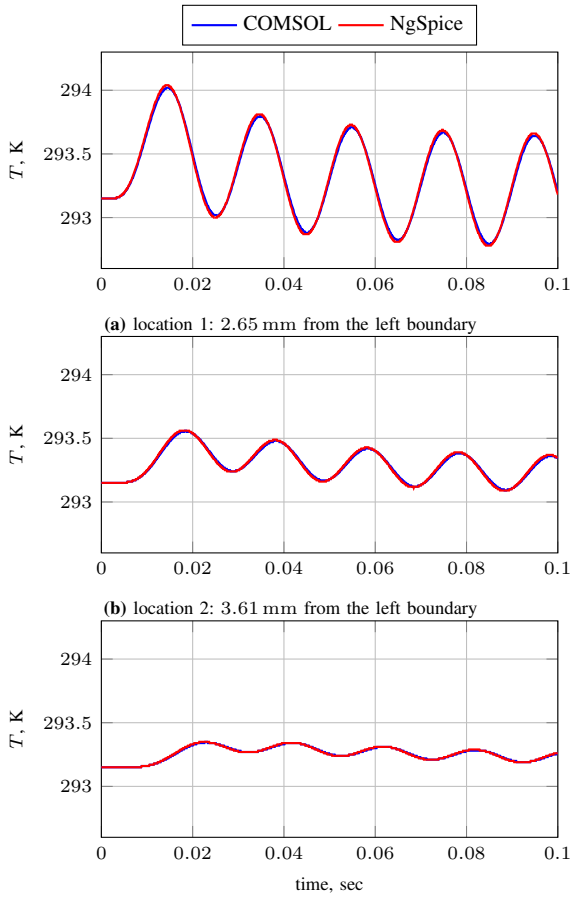

(a) location 1: 2.65 mm from the left boundary

(b) location 2: 3.61 mm from the left boundary

(c) location 3: 4.61 mm from the left boundary

Fig. 15: Temperature as a function of time at three different locations.

1/10 and 5x of copper's, suggesting the same settling behavior observed in Figure 16. Such an insight provided by the circuit view, however, is not easily attainable through directly reading PDEs (in this case eq. (5)). Notice that the settling time in Figure 9 are similar because the same material (copper) was used.

IV. Future Work

We are working on multiphysics design and modeling methodologies to take advantage of the presented unification. It is deemed that the richness of the presented work justifies well for a self-contained publication. Plans for the follow-up work are (1) expanding the scope to 3D fields; (2) deriving the circuit network for linear elastic field using generalized DEC for tensor fields. Both will be a continuation of this multi-part effort.

In the experiments, NgSpice (without involving OpenMP) has shown signs of incapability of handling large circuit networks (i.e. finer meshes in the physical domain). NgSpice solver may crash before a successful run. It is worth mentioning that the goal of this research is not creating a new simulation environment for multiphysics (such as NgSpice). The usage of NgSpice is mainly for validating the proposed

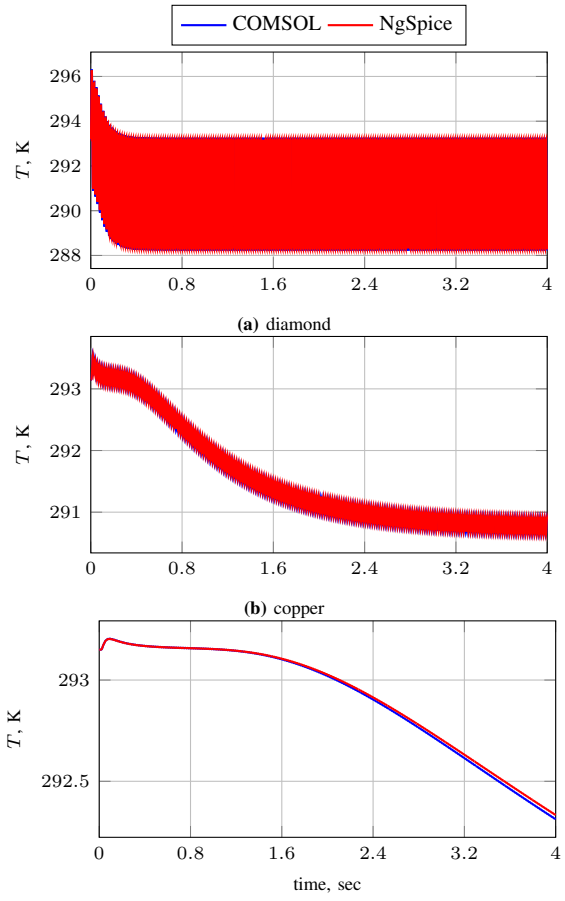

Fig. 16: Temperature as a function of time with three different materials.

equivalent circuits. That being said, it is still worth some effort to study NgSpice solvers in the context of multiphysics modeling. For example, to model 3D fields, even larger circuit networks are to be obtained and a circuit simulator capable of handling these networks is necessary.

V. Conclusions

This paper proposes a unified circuit view of multiphysics FEA in the simulation of engineering objects. It is based on the isomorphism between the topological structures established by discrete calculus and circuit theory. A case study of two physical processes in 2D dynamic conditions in electric machines is presented. Specifically, they are eddy-current and thermal conduction. Lumped elements commonly used in the paper design stage show up in the circuit view. The circuit model of eddy current fields at the mesh level is new. This unified circuit view lowers language barriers between multiphysics. A thorough experimental validation for both physical processes has been undertaken. The results show that the proposed circuit models are correct and have high fidelity. Furthermore, it has been demonstrated that RL and RC time constants used by electrical engineers can be transferred to understand dynamic behavior for other physical processes.

Acknowledgment

The author Baoyun Ge would like to thank the Department of Electrical and Computer Engineering at the University of Florida, where he prepared the presented work.

References

[1] F. Wu, A. M. EL-Refaie, and A. Al-Qarni, "Additively Manufactured Hollow Conductors Integrated With Heat Pipes: Design Tradeoffs and Hardware Demonstration," *IEEE Transactions on Industry Applications*, vol. 57, no. 4, pp. 3632–3642, Jul. 2021.

[2] T. Chowdhury, S. Koushan, A. Al-Qarni, A. El-Refaie, K. Bennion, E. Cousineau, X. Feng, and B. Kekelia, "Thermal Management System for an Electric Machine with Additively Manufactured Hollow Conductors with Integrated Heat Pipes," in *2022 International Conference on Electrical Machines (ICEM)*, Sep. 2022, pp. 1920–1926.

[3] Y. Li, D. Bobba, E. Schubert, H. Ding, and B. Sarlioglu, "Concept of Integration of Axial-Flow Compression Into Electric Machine Design," *IEEE Transactions on Transportation Electrification*, vol. 3, no. 1, pp. 118–129, Mar. 2017.

[4] A. Credo, G. Fabri, M. Villani, and M. Popescu, "Adopting the Topology Optimization in the Design of High-Speed Synchronous Reluctance Motors for Electric Vehicles," *IEEE Transactions on Industry Applications*, vol. 56, no. 5, pp. 5429–5438, Sep. 2020.

[5] F. Guo, M. Salameh, M. Krishnamurthy, and I. P. Brown, "Multimaterial Magneto-Structural Topology Optimization of Wound Field Synchronous Machine Rotors," *IEEE Transactions on Industry Applications*, vol. 56, no. 4, pp. 3656–3667, Jul. 2020.

[6] E. Severson, R. Nilssen, T. Undeland, and N. Mohan, "Dual-Purpose No-Voltage Winding Design for the Bearingless AC Homopolar and Consequent Pole Motors," *IEEE Transactions on Industry Applications*, vol. 51, no. 4, pp. 2884–2895, Jul. 2015.

[7] S. Miric, "Linear-Rotary Bearingless Actuators," Doctoral Thesis, ETH Zurich, 2021.

[8] A. Khamitov and E. L. Severson, "Design of Multi-Phase Combined Windings for Bearingless Machines," *IEEE Transactions on Industry Applications*, vol. 59, no. 3, pp. 3243–3255, May 2023.

[9] L. Xue, V. Galigekere, E. Gurpinar, G.-j. Su, S. Chowdhury, M. Mohammad, and O. Onar, "Modular Power Electronics Approach for High Power Dynamic Wireless Charging System," *IEEE Transactions on Transportation Electrification*, pp. 1–1, 2023.

[10] J. Dai and D. C. Ludois, "A Survey of Wireless Power Transfer and a Critical Comparison of Inductive and Capacitive Coupling for Small Gap Applications," *IEEE Transactions on Power Electronics*, vol. 30, no. 11, pp. 6017–6029, Nov. 2015.

[11] S. Li and C. C. Mi, "Wireless Power Transfer for Electric Vehicle Applications," *IEEE Journal of Emerging and Selected Topics in Power Electronics*, vol. 3, no. 1, pp. 4–17, Mar. 2015.

[12] Y. Sasakawa, S. Takezawa, Y. Sugawara, and Y. Kyotani, "The superconducting MHD-propelled ship YAMATO-1," Apr. 1995.

[13] D. W. Swallom, I. Sadovnik, J. S. Gibbs, H. Gurol, L. V. Nguyen, and H. H. Van Den Bergh, "Magnetohydrodynamic Submarine Propulsion Systems," *Naval Engineers Journal*, vol. 103, no. 3, pp. 141–157, 1991.

[14] I. A. Razi, Q. Le, T. M. Evans, H. A. Mantooth, and Y. Peng, "PowerSynth 2: Physical Design Automation for High-Density 3D Multi-Chip Power Modules," *IEEE Transactions on Power Electronics*, pp. 1–16, 2022.

[15] Y. Zhou, Y. Jin, Y. Chen, H. Luo, W. Li, and X. He, "Graph-Model-Based Generative Layout Optimization for Heterogeneous SiC Multichip Power Modules With Reduced and Balanced Parasitic Inductance," *IEEE Transactions on Power Electronics*, vol. 37, no. 8, pp. 9298–9313, Aug. 2022.

[16] P. Ning, H. Li, Y. Huang, and Y. Kang, "Review of power module automatic layout optimization methods in electric vehicle applications," *Chinese Journal of Electrical Engineering*, vol. 6, no. 3, pp. 8–24, Sep. 2020.

[17] B. Ge, "A Unified Circuit View of Multiphysics Finite Element Analysis via Discrete Exterior Calculus Part I: 2D Static Fields," in *2023 IEEE Energy Conversion Congress and Exposition (ECCE)*, Oct. 2023, pp. 4544–4551.

[18] A. N. Hirani, "Discrete Exterior Calculus," Ph.D. dissertation, California Institute of Technology, 2003.

[19] M. Desbrun, A. N. Hirani, M. Leok, and J. E. Marsden, "Discrete Exterior Calculus," Aug. 2005.
[20] N. Bell and A. N. Hirani, "PyDEC: Software and Algorithms for Discretization of Exterior Calculus," *ACM Transactions on Mathematical Software*, vol. 39, no. 1, pp. 1–41, Nov. 2012.
[21] L. J. Grady and J. R. Polimeni, *Discrete Calculus: Applied Analysis on Graphs for Computational Science*, 2010th ed. London ; New York: Springer, Aug. 2010.
[22] E. Tonti, *The Mathematical Structure of Classical and Relativistic Physics: A General Classification Diagram*, 2013th ed. New York: Birkhäuser, Sep. 2013.
[23] D. L. Logan, *A First Course in the Finite Element Method*, 5th ed. Stamford, CT: CL Engineering, Jan. 2011.
[24] P. I. Kattan, *MATLAB Guide to Finite Elements: An Interactive Approach*, 2nd ed. Berlin ; New York: Springer, Mar. 2007.
[25] W. Qin, M. Cheng, X. Zhu, Z. Wang, and W. Hua, "Electromagnetic induction with time-varying magductance under constant magnetic field," *AIP Advances*, vol. 14, no. 2, p. 025115, Feb. 2024.